

See discussions, stats, and author profiles for this publication at: <https://www.researchgate.net/publication/319081348>

# Enhanced bovine serum albumin absorption on the N-hydroxysuccinimide activated graphene oxide and its corresponding cell affinity

**Article** in *Materials Science and Engineering C* · August 2017

DOI: 10.1016/j.msec.2017.08.044

CITATIONS

0

READS

82

**6 authors**, including:



**Kun Xiong**

Southwest University of Science and Technology

**17** PUBLICATIONS **102** CITATIONS

[SEE PROFILE](#)



**Tingting Wu**

South China University of Technology

**6** PUBLICATIONS **1** CITATION

[SEE PROFILE](#)



**Haishan Shi**

Jinan University (Guangzhou, China)

**17** PUBLICATIONS **66** CITATIONS

[SEE PROFILE](#)



**Minhao Yan**

Southwest University of Science and Technology

**46** PUBLICATIONS **357** CITATIONS

[SEE PROFILE](#)

**Some of the authors of this publication are also working on these related projects:**



Micro/nano-biomaterials as the carriers of drugs, factors and ions for the treatments of myelitis and osteoarthritis [View project](#)



Bioactive ions doped calcium phosphates for bone regeneration [View project](#)



# Enhanced bovine serum albumin absorption on the N-hydroxysuccinimide activated graphene oxide and its corresponding cell affinity

Kun Xiong<sup>a,\*</sup>, Qingbo Fan<sup>a,1</sup>, Tingting Wu<sup>b</sup>, Haishan Shi<sup>c</sup>, Lin Chen<sup>a</sup>, Minhao Yan<sup>a</sup>

<sup>a</sup> State Key Laboratory Cultivation Base for Nonmetal Composites and Functional Materials, Southwest University of Science and Technology, Mianyang 621010, China

<sup>b</sup> National Engineering Research Center for Tissue Restoration and Reconstruction, Guangzhou 510006, China

<sup>c</sup> College of Chemistry and Materials, Jinan University, Guangzhou 510632, China

## ARTICLE INFO

### Keywords:

Graphene oxide  
Active ester  
EDC/NHS  
BSA absorption  
Cell adhesion

## ABSTRACT

By successively reacting with *N*-(3-Dimethylaminopropyl)-*N'*-ethylcarbodiimide hydrochloride (EDC) and *N*-hydroxysuccinimide (NHS), the carboxyl on the graphene oxide (GO) surface was successfully activated into NHS active ester. In this study, bovine serum albumin (BSA) was selected as a model protein, used for studying the protein absorption capacity of the NHS activated GO (GO-EDC-NHS). Approximately 12.75 mg of BSA could be covalent bonded onto the GO-EDC-NHS surface (BSA-CB-GO), whereas only 6.83 mg of BSA physical absorbed onto the GO surface (BSA-NB-GO). With a 168 h of phosphate buffer saline (PBS) soaking, the BSA accumulative desorption ratio, which was accordingly assigned to the BSA-NB-GO and the BSA-CB-GO, was separately 29.91 wt% and 2.95 wt%. Consequently, it proved GO-EDC-NHS exhibited more stable and stronger BSA absorption capacity. As compared to the mouse bone marrow mesenchymal stem cells (mBMSCs) cultivated on the BSA-NB-GO surface, the immunofluorescence staining images showed that more vinculin and integrin  $\alpha 5$  were visible in the mBMSCs cultivated on the BSA-CB-GO surface, they also produced more distinct stress fibers and actin-containing microfilaments. In summary, BSA-CB-GO possesses an excellent cell affinity, which can be considered as a promising functional material used for promoting the bone remodeling.

## 1. Introduction

Since the growing demands for bone grafting, hybrid materials and composite scaffolds have received considerable attentions in recent years, they not only can provide platforms for cell adhesion and growth, but also delivery various bioactive ingredients to promote bone regeneration [1–8]. In the bone remodeling process, the cell adhesion as well as the cell spreading is the initial interaction between the cells and the materials, which can affect the subsequent cell behaviors, such as cell proliferation and cell differentiation [9]. It is well known that cells prefer adhering to the places where are rich in cell adhesive proteins, so it means the cell affinity actually depends on the protein absorption capacity of the materials surface [10,11]. It has been reported that the protein absorption capacity are affected by the material surface topography as well as its surface wettability [12–17]. Thus, various surface modification techniques are used to improve the materials surface properties [18].

Graphene oxide (GO), a typical sp<sup>2</sup> carbon nanomaterials, which has exhibited great potentials to be applied to the biomedical fields including bone tissue engineering [19–25], drug/gene delivery [26–32]

and photothermal therapy [33–37]. Because of existence of many oxygen-containing functional groups (such as hydroxyl, carboxyl, carbonyl, etc.) on its surface, GO is able to induce proteins to absorb onto its surface via the  $\pi$ -stacking interaction, electrostatic interaction or hydrogen bonding [38,39]. Consequently, GO is usually added into the biopolymers to improve their cell affinity [9,25,40–43]. Nevertheless, as compared to the chemical bonding, the physical absorption process is dynamic and uncontrollable, which is easy to be influenced by the microenvironment change, so the protein absorption capacity of GO is limited in this case.

Here we tried to use *N*-(3-Dimethylaminopropyl)-*N'*-ethylcarbodiimide hydrochloride (EDC) and *N*-hydroxysuccinimide (NHS) to activate the carboxyl on the GO surface, and the NHS active esters would be produced. Since the amino group in protein could react with the NHS active ester, proteins were easily covalent bonded onto the NHS activated GO (GO-EDC-NHS) surface via the amide linkage. Albumin is the most abundant protein in blood, while 55 wt% of the total blood proteins is bovine serum albumin (BSA) [44]. Therefore, BSA was selected as a model protein, used for studying the protein absorption capacity and absorption stability of the GO-EDC-NHS, the untreated GO was

\* Corresponding author.

E-mail address: [quentin\\_xiong@swust.edu.cn](mailto:quentin_xiong@swust.edu.cn) (K. Xiong).

<sup>1</sup> The first two authors contribute equally to this work.

considered as the control group. Thereafter, the mouse bone marrow mesenchymal stem cells (mBMSCs) were cultivated on the silicon wafer of which surface was covered by BSA covalent bonded GO (BSA-CB-GO), the corresponding cell adhesion as well as the cell spreading behaviors were investigated in detail.

## 2. Experimental section

### 2.1. Preparations of the GO and the GO-EDC-NHS

GO was prepared by the modified Hummers method [45]. In this study, the flake graphite powder (natural grade, ~8000 mesh, 99.95% metal based) was used as a starting material, which was purchased from Shanghai Aladdin Biological Technology Co., Ltd. Afterwards, the as-prepared GO suspension was freeze-dried and the GO powders were collected. With a 2 h of ultrasonic dispersion, 50 mg of the as-prepared GO powders were well dispersed in 50 mL ultrapure water, and its pH was adjusted to 6.1 by using 2-(N-Morpholino)ethanesulfonic acid (MES, CAS: 4432-31-9, ≥99.5%, Aladdin, China) buffer solution (500 mM, pH ~ 6.1). In addition, the EDC (CAS: 25952-53-8, ≥98%, Sigma, USA) and the NHS (CAS: 6066-82-6, 98%, Sigma, USA) were separately dissolved in MES buffer solution (50 mM, pH ~ 6.1), the final concentration was corresponding to 10 mg/mL and 50 mg/mL, and their pH were all kept at 6.1. As illustrated in the preparation schematic drawing of GO-EDC-NHS (Fig. 1), under a vigorous stirring condition, 30 mL of EDC solution was firstly added into 50 mL of GO suspension to make the carboxyls on GO surface to be activated into active esters, and the reaction time was 15 min. Nevertheless, the above active esters were easy to hydrolysis in a short time, so 25 mL of NHS solution was subsequently added to make the active ester structure stable. The GO-EDC-NHS suspension was centrifuged, and the GO-EDC-NHS precipitates were rinsed three times with MES buffer solution (50 mM, pH ~ 6.1) in order to remove the residue EDC, NHS as well as the urea byproducts [46]. Finally, the precipitates were freeze-dried to obtain the GO-EDC-NHS powders.

### 2.2. The *in vitro* BSA absorption experiments

The BSA absorption process was described as follows, 10 mg of GO-EDC-NHS powders were redispersed in 25 mL of MES buffer solution (50 mM, pH ~ 6.1), and 50 mg of BSA powders were completely dissolved in 5 mL of MES buffer solution (50 mM, pH ~ 6.1). Thereafter, the as-prepared BSA solution was added into the GO-EDC-NHS suspension, and they were set in a shaker for 2 h (200 rpm, room temperature). As depicted in Fig. 1, the BSA (≥95%, Cat.no. 36101ES25, Shanghai Yeasen Biotechnology Co., Ltd., China) could be bonded to GO-EDC-NHS via the amide linkage and formed the BSA-CB-GO. When other parameters were kept in constant, the BSA anchored onto the GO surface through the physical absorption (BSA-NB-GO) was considered as the control group. The BSA-CB-GO and the BSA-NB-GO precipitates were collected by centrifugation, and then the MES buffer solution (50 mM, pH ~ 6.1) was used to wash them once. All the supernatants and washing liquids were collected for testing. According to the protocol of Coomassie brilliant blue protein assay, the amount of the

residual BSA in the MES buffer solution was determined by absorbance at 595 nm in the UV-Vis absorption spectrum [47] (UV-3150, Shimadzu, Japan). Because the original BSA amount as well as the residual BSA amount is known, it is easy to calculate the amount of BSA absorbed on materials surfaces.

In order to investigate the BSA binding stability, 20 mL of Dulbecco's phosphate buffer saline (PBS, Sigma, USA) were separately added to make the above BSA-CB-GO as well as BSA-NB-GO precipitates to be completely submerged. At predetermined time intervals (2, 4, 8, 24, 72, 120, 168 h), 1 mL of supernatant was collected for testing, and equal fresh PBS was supplemented. Each group contains three parallel samples.

### 2.3. Characterizations

The phase composition of the samples was characterized by X-ray diffractometer (XRD, X'Pert PRO, PANalytical, The Netherlands) using a Cu K $\alpha$  source ( $\lambda = 1.5406 \text{ \AA}$ ). The morphology of the samples was observed via a high-resolution transmission electron microscope (HRTEM, LIBRA 220FE, ZEISS, Germany). The chemical compositions of the samples were determined by X-ray photoelectron spectroscopy (XPS, ESCALAB 250Xi, Thermo Scientific, USA), and the binding energies were normalized to the signal for adventitious C 1s at 284.8 eV. The functional groups of the samples were determined by Fourier transform infrared spectrometer (FTIR, Spectrum One, PerkinElmer, USA). The surface charges of the samples were tested via a zeta potential analyzer (NanoBrook Omni, Brookhaven, USA).

### 2.4. Cell culture experiments

The primary mBMSCs (Cat.no. CRL-12424, ATCC, USA) were subcultivated in a cell incubator at 37 °C with a 5% CO<sub>2</sub> humidified atmosphere. As mBMSCs were almost confluent in the bottom of cell culture flasks, 0.25% trypsin/EDTA (Cat.no. 25200-056, Gibco, USA) was added to make them detachment. Whereafter, the detached mBMSCs were collected and stored in a liquid nitrogen container. The mBMSCs after 7 times of passages were used for the following cell culture experiments. High-glucose Dulbecco's Modified Eagle's Medium (H-DMEM, Cat.no. 11965-092, Gibco, USA) with 10 vol% of fetal bovine serum (FBS, Cat.no. 10099-141, Gibco, USA) was selected for culturing the mBMSCs.

### 2.5. Immunofluorescence staining experiments

The sterilized silicon wafers of which surface was covered by the BSA-CB-GO (20 kGy of  $\gamma$ -ray irradiation) were set into a 24-well culture plate, and the mBMSCs were seeded on their surface according to a cell density of  $3 \times 10^4$  cells/well. Subsequently, 1 mL/well of H-DMEM medium with 10 vol% of FBS was added, the culture plates were transferred into a cell incubator (37 °C with a 5% CO<sub>2</sub> humidified atmosphere) and kept for 48 h. In this study, the silicon wafers with a BSA-NB-GO surface layer were considered as the control group. Thereafter, the cell culture medium was removed and the silicon wafers were rinsed twice with PBS. Afterwards, the above silicon wafers were

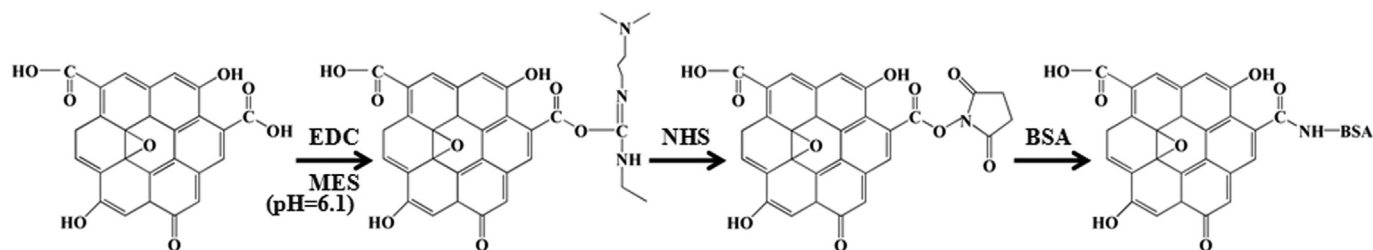


Fig. 1. The schematic drawing of the preparation of GO-EDC-NHS and BSA-CB-GO.

soaked in 4 vol% paraformaldehyde solution for 20 min to make the mBMSCs fixation. Fixed mBMSCs were permeabilized with 0.1 vol% Triton X-100 (Sigma Aldrich, USA) for 10 min. According to the manufacturer's protocols, actin microfilaments were identified by Alexa-Fluor® 488 phalloidin (AAT Bioquest, USA), nuclei were stained by DAPI (Beyotime, China), focal adhesion (FA) were identified by staining of vinculin using anti-vinculin antibody (Abcam, USA) and Cy3-conjugated Affinipure Goat Anti-Rabbit IgG(H + L) (Protein Tech Group, USA), integrin  $\alpha 5$  were identified by anti-integrin  $\alpha 5$  antibody (Abcam, USA) and Cy3-conjugated Affinipure Goat Anti-Rabbit IgG(H + L) (Protein Tech Group, USA). Fluorescence images of the F-actin, vinculin and integrin  $\alpha 5$  distributions of mBMSCs were analyzed by a confocal laser scanning microscope (CLSM, TCS SP5, Leica Microsystems, Germany). In addition, based on the fluorescence images, the quantitative analysis of the vinculin and the integrin  $\alpha 5$  were performed by using the software (Image J, National Institutes of Health, USA).

### 2.6. Statistical analysis

Quantitative data were presented as mean  $\pm$  standard deviation and statistical analyses were performed using a one-way analysis of variance (one-way ANOVA). A comparison between the two means was made by using the Tukey's test, with statistical significance set at  $P < 0.05$ .

## 3. Results and discussions

The FTIR spectrum of GO was presented in Fig. 2(a), the absorption peaks situated at 3400, 1727, 1621, 1405, 1225 and 1053  $\text{cm}^{-1}$ , which were separately corresponding to the O–H stretching vibration, the C=O stretching vibration of carboxyl or carbonyl, the O–H deformation vibration, the C–O stretching vibration of carboxyl, the C–O stretching vibration of epoxy group, and the C–O stretching vibration of alkoxy at the edges of the GO [48]. As displayed in the FTIR spectrum of GO-EDC-NHS (Fig. 2(b)), the absorption peaks separately situated at 2924, 2853 and 1466  $\text{cm}^{-1}$  was accordingly assigned to the  $-\text{CH}_2$  asymmetric stretching vibration, symmetric stretching vibration and scissoring vibration. The absorption peak situated at 1631  $\text{cm}^{-1}$  was assigned to the C=O stretching vibration of amide I [49]. In addition, the diffraction peaks of succinimide (JCPDS card no. 00-007-0745) were observed in the XRD pattern of GO-EDC-NHS (Fig. 3), which proved the successful formation of NHS active ester on GO surface. The residue NHS was probably ascribed to the hydrolysis of the active esters. In the FTIR spectrum of BSA-CB-GO (Fig. 2(c)), the peak situated at 1653  $\text{cm}^{-1}$  was assigned to the C=O stretching vibration of amide I, which exhibited a red shift as compared to the C=O stretching vibration peak in the FTIR of GO-EDC-NHS (Fig. 2(b)). Furthermore, a new absorption peak

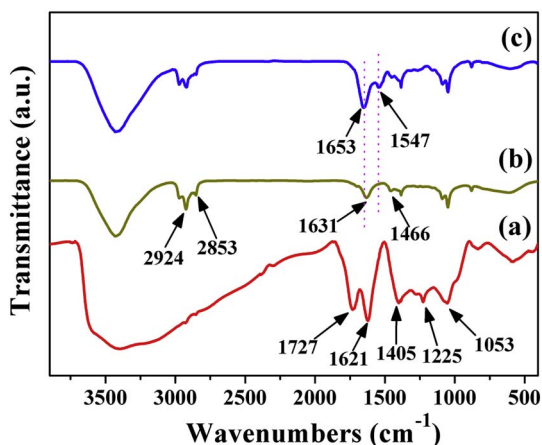


Fig. 2. The FTIR spectra of (a) GO, (b) GO-EDC-NHS and (c) BSA-CB-GO.

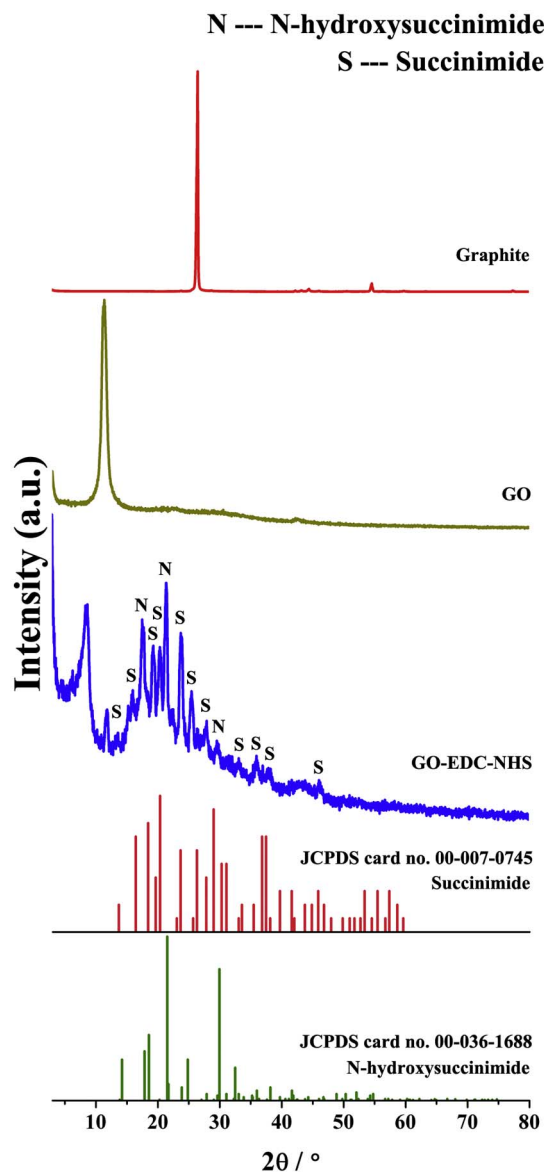


Fig. 3. XRD patterns of graphite, GO and GO-EDC-NHS.

situated at 1547  $\text{cm}^{-1}$  was observed in the FTIR spectrum of BSA-CB-GO, which should be assigned to the C–N stretching vibration and the N–H deformation vibration of amide II [49]. Therefore, it confirmed BSA successfully anchored onto the GO-EDC-NHS surface via the amide linkage.

As shown in Fig. 4(a), the C 1s core level XPS spectrum of GO can be fitted with 4 peaks, including two distinct peaks, at 284.78 eV and 286.84 eV, and two small peaks, at 287.71 eV and 289 eV. The peak situated at 284.78 eV arises from the nonoxygenated ring (C–C and C=C bond), whereas the peak situated at 286.84 eV probably corresponds to the C–O bond [50]. In addition, the small peak situated at 287.71 eV is assigned to the C=O bond of carbonyl, and the peak situated at 289 eV belongs to the O–C = O bond of carboxyl ( $-\text{COOH}$ ) [51]. After successively reacting with the EDC and the NHS, besides the C–C bond, C–O bond and C=O bond associated peaks, two new peaks situated at 285.51 eV and 288.57 eV were found in the C 1s core level XPS spectrum of GO-EDC-NHS (Fig. 4(b)). The peak situated at 285.51 eV should be assigned to the C–N bond of NHS, which can be proved by Fig. 4(c). Moreover, the peak situated at 288.57 eV represents the O–C = O bond of ester ( $-\text{COO}-$ ), its corresponding binding energy is about 0.43 eV smaller than the  $-\text{COOH}$  because of an electron donation

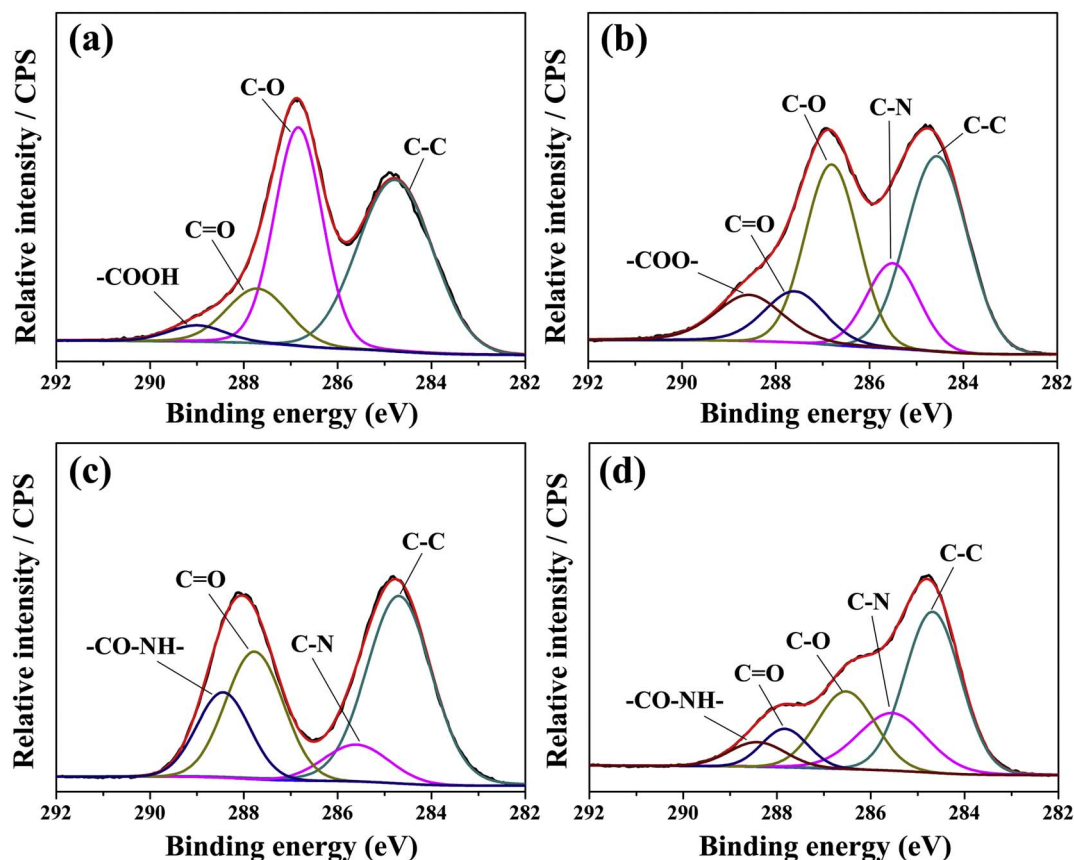


Fig. 4. The C 1 s core level XPS spectra of (a) GO, (b) GO-EDC-NHS, (c) NHS and (d) BSA-CB-GO.

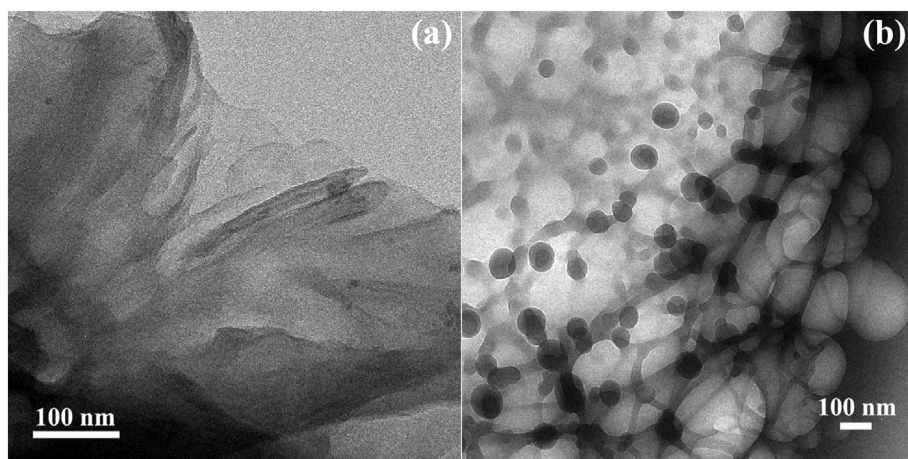


Fig. 5. TEM images of (a) GO-EDC-NHS and (b) BSA-CB-GO.

Table 1

Zeta potentials of the BSA, GO and GO-EDC-NHS (pH = 6.1, in the MES solution, n = 3).

Samples	BSA	GO	GO-EDC-NHS
Zeta potential (mV)	$-11.69 \pm 0.23$	$-20.11 \pm 0.37$	$-13.01 \pm 0.61$

from the adjacent nitrogen atom [52]. Therefore, it also confirms the carboxyls are really activated into the active esters, which is in good accordance with the FTIR and the XRD analysis results. In the C 1 s core level XPS spectrum of NHS (Fig. 4(c)), the peak situated at 288.44 eV should be assigned to the amide bond ( $-\text{CO}-\text{NH}-$ ). Furthermore, the  $-\text{CO}-\text{NH}-$  peak also can be observed in the C 1 s core level XPS spectrum of BSA-CB-GO (Fig. 4(d)). More importantly, the disappearance of

$-\text{COO}-$  further proves BSA is covalent bonding onto the GO-EDC-NHS surface through the NHS active ester reaction with the amino group. As displayed in the TEM image of the BSA-CB-GO (Fig. 5(b)), many spherical BSA well anchored onto the GO-EDC-NHS surface.

Based on the testing results of Coomassie brilliant blue protein assay, the BSA-CB-GO contains 12.75 mg of BSA, whereas the BSA-NB-GO only contains 6.83 mg of BSA, so it indicates the BSA absorption capacity of GO can be significantly promoted via the activation of carboxyl into NHS active ester. As listed in Table 1, the zeta potentials of the BSA, GO and GO-EDC-NHS (pH = 6.1, in the MES solution) are  $-11.69 \pm 0.23$  mV,  $-20.11 \pm 0.37$  mV and  $-13.01 \pm 0.61$  mV, respectively. It is well known that BSA is a kind of acidic protein, and its isoelectric point is 4.7 [53], so it is reasonable that BSA possesses negative charge at pH = 6.1. In this case, since they all show the negative

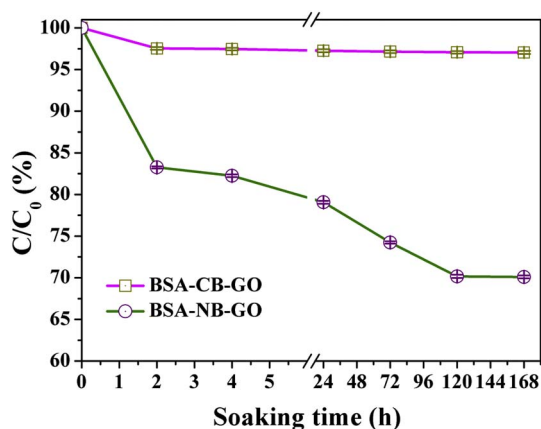


Fig. 6. The BSA desorption performance of the BSA-CB-GO and the BSA-NB-GO ( $n = 3$ ).

surface charge, the electrostatic repulsion will affect the physical absorption of BSA. Nevertheless, it has less influence on BSA absorbing onto the GO-EDC-NHS surface via the amide linkage, so it well explains why BSA-NB-GO contains fewer BSA than BSA-CB-GO. In order to investigate their BSA binding stability, the BSA-NB-GO and the BSA-CB-GO were soaked in the PBS, respectively. As shown in Fig. 6, with a 2 h of PBS soaking, about 16.75 wt% of BSA detached from BSA-NB-GO, whereas only 2.46 wt% of BSA detached from BSA-CB-GO. As the soaking time prolonged to 168 h, the BSA accumulative desorption ratio, which was accordingly assigned to the BSA-NB-GO and the BSA-CB-GO, was separately 29.91 wt% and 2.95 wt%. Thus, it indicated the BSA which anchored onto the GO-EDC-NHS surface via the amide linkage is more stable than the physical absorbed BSA. Only the carboxyls on the GO surface were activated, so BSA also could bind to other oxygen containing functional groups via the physical ways. Therefore, for BSA-CB-GO, the initial released BSA was probably ascribed to the physical desorption.

As presented in Fig. 7, no matter being cultivated on the BSA-NB-GO surface or the BSA-CB-GO surface, the vinculin could be clearly observed in the mBMSCs. Nevertheless, as compared to the mBMSCs cultivated on the BSA-NB-GO surface, the expression level of the vinculin, which was assigned to the mBMSCs seeded on the BSA-CB-GO surface, was significantly up-regulated, indicating more FA formed on the BSA-CB-GO surface. FA is a multi-protein complex which possess the sub-cellular structure, and it can form the mechanical linkages between intracellular actin bundles and extracellular matrix (ECM) [54]. Vinculin is a membrane-cytoskeletal protein in FA, which mainly participates in the linkages between cell adhesion membranous molecules,

integrins and actin filaments [55]. Moreover, vinculin plays positive roles in initiating and establishing cell adhesion, controlling the cell shape as well as cytoskeleton development [56]. W.H. Goldmann had reported the loss of vinculin could prevent the cell adhesion and spreading, the formation of stress fibers as well as the extension of lamellipodia and filopodia [57]. Because more vinculins were produced in the mBMSCs when they were cultivated on the BSA-CB-GO surface, it means BSA-CB-GO contributes to cell adhesion.

Integrin is a heterodimer consisting of two subunits ( $\alpha$  and  $\beta$ ), and it also can mediate cell adhesion and cell spreading via the combination of the integrin  $\alpha5\beta1$  (trans-membrane receptor) and the fibronectins (FNs, a key cell adhesive protein) which are absorbed on materials surface [58–60]. Integrin  $\alpha5\beta1$  is composed of the  $\alpha5$  subunit and the  $\beta1$  subunit. As shown in Fig. 8, the area of the integrin  $\alpha5$ , which was assigned to the mBMSCs cultivated on the BSA-CB-GO surface, was remarkable larger than that assigned to the mBMSCs cultivated on the BSA-NB-GO surface, implying the mBMSCs cultivated on the BSA-CB-GO surface had a significant higher expression of integrin  $\alpha5$ . Moreover, as compared to the mBMSCs attached on the BSA-NB-GO surface, the mBMSCs attached on the BSA-CB-GO surface could produce more distinct stress fibers as well as actin-containing microfilaments, and their cytoskeleton also obviously expanded (Fig. 9).

From the above, it confirmed the mBMSCs preferred the BSA rich-in surface. As compared to the BSA-NB-GO, the BSA-CB-GO could further improve the cell adhesion and the cell spreading behaviors, which was probably ascribed to its remarkable enhanced BSA absorption capacity.

#### 4. Conclusions

The GO with active esters were successfully prepared by using the EDC/NHS to activate its surface carboxyls, and BSA could anchor onto the GO-EDC-NHS surface via the amide linkage. In comparison with the GO, GO-EDC-NHS exhibited a stronger BSA absorption capacity and better BSA binding stability. Moreover, the mBMSCs cultivated on the BSA-CB-GO surface could produce more vinculin and integrin  $\alpha5$ , implying the BSA-CB-GO possessed better cell adhesion and cell spreading behaviors, which can be used to improve the cell affinity of bone repair materials.

#### Acknowledgements

This work is financially supported by National Nature Science Foundation of China (Grant No. 51402247); Sichuan Education Department Innovation Team Foundation (16zd1104); Sichuan Province Science Foundation for Young Scientists (No. 15zs2111); Open Project of State Key Laboratory Cultivation Base for Nonmetal

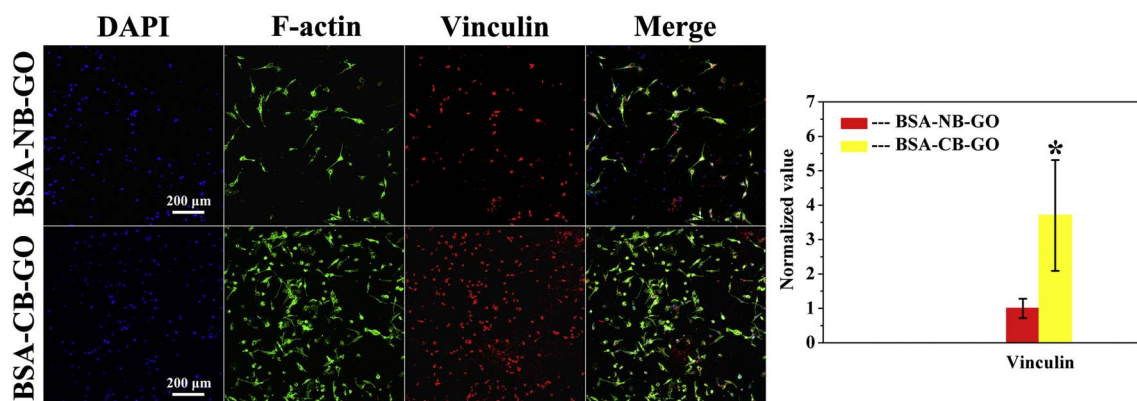
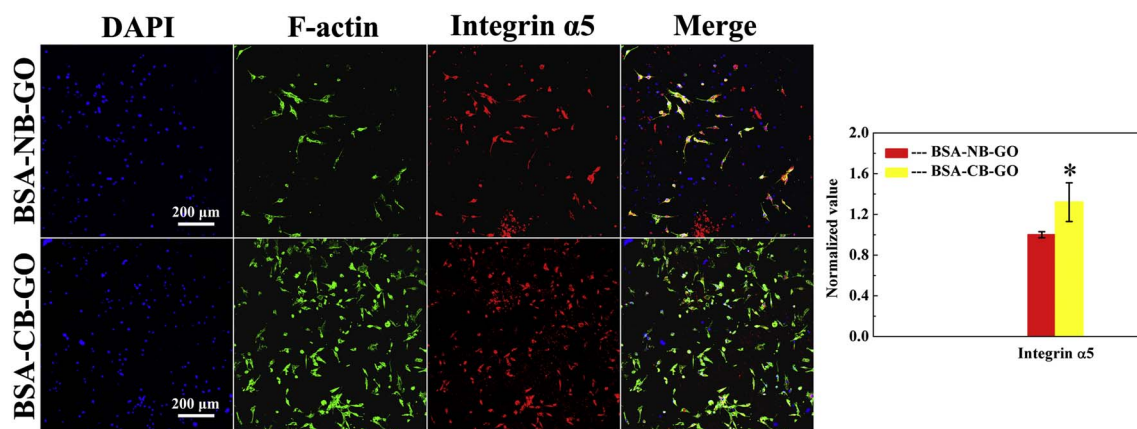
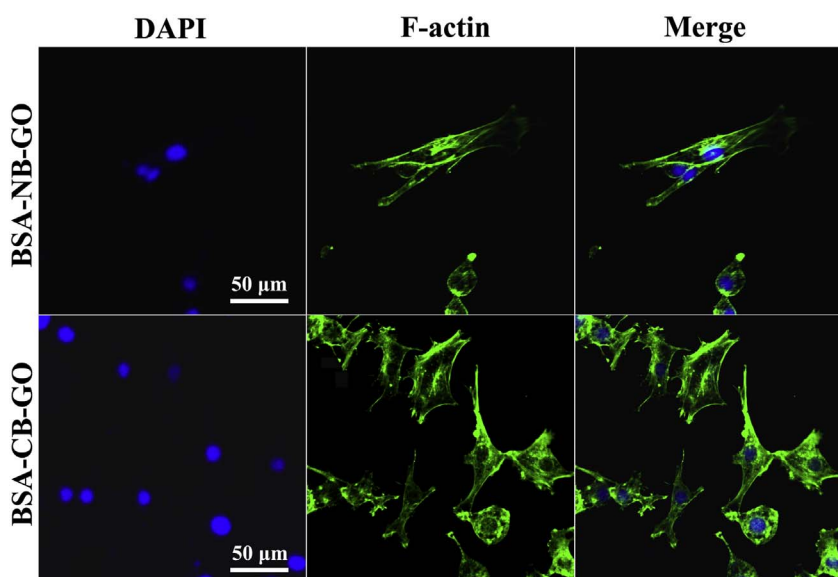


Fig. 7. Immunofluorescence staining images of DAPI (blue), F-actin (green), vinculin (red) and their merged images of the mBMSCs separately cultivated on the BSA-NB-GO surface and the BSA-CB-GO surface for 48 h; the quantitative analysis data for the expression of the vinculin in mBMSCs, which were quantified by measuring the areas > 250 cells. The data were presented as mean  $\pm$  S.D.,  $n = 4$ . \*The BSA-CB-GO compared with the BSA-NB-GO,  $P < 0.01$ . The BSA-NB-GO was considered as the control group. (For interpretation of the references to colour in this figure legend, the reader is referred to the web version of this article.)



**Fig. 8.** Immunofluorescence staining images of DAPI (blue), F-actin (green), integrin  $\alpha 5$  (red) and their merged images of the mBMSCs separately cultivated on the BSA-NB-GO surface and the BSA-CB-GO surface for 48 h; the quantitative analysis data for the expression of the integrin  $\alpha 5$  in mBMSCs, which were quantified by measuring the areas > 250 cells. The data were presented as mean  $\pm$  S.D.,  $n = 4$ . \*The BSA-CB-GO compared with the BSA-NB-GO,  $P < 0.01$ . The BSA-NB-GO was considered as the control group. (For interpretation of the references to colour in this figure legend, the reader is referred to the web version of this article.)



**Fig. 9.** The fluorescence images of DAPI (blue), F-actin (green) and their merged images of the mBMSCs separately cultivated on the BSA-NB-GO surface and the BSA-CB-GO surface for 48 h. (For interpretation of the references to colour in this figure legend, the reader is referred to the web version of this article.)

Composites and Functional Materials (No.13ZXFK11); Doctoral Research Foundation of Southwest University of Science and Technology (No. 14zx7119); Postgraduate Innovation Fund Project of Southwest University of Science and Technology (No. 16ycx020).

## References

- [1] K.-C. Hung, C.-S. Tseng, L.-G. Dai, S.-h. Hsu, Water-based polyurethane 3D printed scaffolds with controlled release function for customized cartilage tissue engineering, *Biomaterials* 83 (2016) 156–168.
- [2] Q. Yao, J.G.L. Cosme, T. Xu, J.M. Miszuk, P.H.S. Picciani, H. Fong, H. Sun, Three dimensional electrospun PCL/PLA blend nanofibrous scaffolds with significantly improved stem cells osteogenic differentiation and cranial bone formation, *Biomaterials* 115 (2017) 115–127.
- [3] X. Shen, Y. Zhang, Y. Gu, Y. Xu, Y. Liu, B. Li, L. Chen, Sequential and sustained release of SDF-1 and BMP-2 from silk fibroin-nanohydroxyapatite scaffold for the enhancement of bone regeneration, *Biomaterials* 106 (2016) 205–216.
- [4] M. Mehrali, A. Thakur, C.P. Pennisi, S. Talebian, A. Arpanaei, M. Nikkha, A. Dolatshahi-Pirouz, Nanoreinforced hydrogels for tissue engineering: biomaterials that are compatible with load-bearing and electroactive tissues, *Adv. Mater.* 29 (2017) 1603612.
- [5] S. Wang, D.H.R. Kempen, G.C.W. de Ruiter, L. Cai, R.J. Spinner, A.J. Windebank, M.J. Yaszemski, L. Lu, Molecularly engineered biodegradable polymer networks with a wide range of stiffness for bone and peripheral nerve regeneration, *Adv. Funct. Mater.* 25 (2015) 2715–2724.
- [6] X. Hu, Y. Wang, Y. Tan, J. Wang, H. Liu, Y. Wang, S. Yang, M. Shi, S. Zhao, Y. Zhang, Q. Yuan, A difunctional regeneration scaffold for knee repair based on aptamer-directed cell recruitment, *Adv. Mater.* 29 (2017) 1605235.
- [7] R.M. Raftery, D.P. Walsh, I.M. Castaño, A. Heise, G.P. Duffy, S.-A. Cryan, F.J. O'Brien, Delivering nucleic-acid based nanomedicines on biomaterial scaffolds for orthopedic tissue repair: challenges, progress and future perspectives, *Adv. Mater.* 28 (2016) 5447–5469.
- [8] T.G. Kim, H. Shin, D.W. Lim, Biomimetic scaffolds for tissue engineering, *Adv. Funct. Mater.* 22 (2012) 2446–2468.
- [9] J. Song, H. Gao, G. Zhu, X. Cao, X. Shi, Y. Wang, The preparation and characterization of polycaprolactone/graphene oxide biocomposite nanofiber scaffolds and their application for directing cell behaviors, *Carbon* 95 (2015) 1039–1050.
- [10] F. Wu, W. Chen, B. Gillis, C. Fischbach, L.A. Estroff, D. Gourdon, Protein-crystal interface mediates cell adhesion and proangiogenic secretion, *Biomaterials* 116 (2017) 174–185.
- [11] Y. Arima, H. Iwata, Effect of wettability and surface functional groups on protein adsorption and cell adhesion using well-defined mixed self-assembled monolayers, *Biomaterials* 28 (2007) 3074–3082.
- [12] C. Crowley, P. Klanrit, C.R. Butler, A. Varanou, M. Platé, R.E. Hynds, R.C. Chambers, A.M. Seifalian, M.A. Birchall, S.M. Janes, Surface modification of a POSS-nanocomposite material to enhance cellular integration of a synthetic bioscaffold, *Biomaterials* 83 (2016) 283–293.
- [13] M.F.A. Cutiongco, S.H. Goh, R. Aid-Launais, C. Le Visage, H.Y. Low, E.K.F. Yim, Planar and tubular patterning of micro and nano-topographies on poly(vinyl alcohol) hydrogel for improved endothelial cell responses, *Biomaterials* 84 (2016) 184–195.
- [14] A. Ferrari, M. Cecchini, M. Serresi, P. Faraci, D. Pisignano, F. Beltram, Neuronal polarity selection by topography-induced focal adhesion control, *Biomaterials* 31 (2010) 4682–4694.
- [15] N.N.T. Le, S. Zorn, S.K. Schmitt, P. Gopalan, W.L. Murphy, Hydrogel arrays formed via differential wettability patterning enable combinatorial screening of stem cell behavior, *Acta Biomater.* 34 (2016) 93–103.
- [16] M. Nikkha, F. Edalat, S. Manoucheri, A. Khademhosseini, Engineering microscale

- topographies to control the cell–substrate interface, *Biomaterials* 33 (2012) 5230–5246.
- [17] S. Xu, Z. Zhou, M. Gao, C. Zou, Y. Che, B. Cody, X. Zou, L. Zhou, Bioadaptive nanorod topography of titanium surface to control cell behaviors and osteogenic differentiation of preosteoblast cells, *J. Mater. Sci. Technol.* 32 (2016) 944–949.
- [18] H.C. Guo, E. Ye, Z. Li, M.-Y. Han, X.J. Loh, Recent progress of atomic layer deposition on polymeric materials, *Mater. Sci. Eng. C* 70 (2017) 1182–1191.
- [19] H. Xie, T. Cao, J.V. Gomes, A.H. Castro Neto, V. Rosa, Two and three-dimensional graphene substrates to magnify osteogenic differentiation of periodontal ligament stem cells, *Carbon* 93 (2015) 266–275.
- [20] W. Nie, C. Peng, X. Zhou, L. Chen, W. Wang, Y. Zhang, P.X. Ma, C. He, Three-dimensional porous scaffold by self-assembly of reduced graphene oxide and nano-hydroxyapatite composites for bone tissue engineering, *Carbon* 116 (2017) 325–337.
- [21] M. Mehrli, E. Moghaddam, S.F.S. Shirazi, S. Baradaran, M. Mehrli, S.T. Latibari, H.S.C. Metselaar, N.A. Kadri, K. Zandi, N.A. Abu Osman, Synthesis, mechanical properties, and in vitro biocompatibility with osteoblasts of calcium silicate-reduced graphene oxide composites, *ACS Appl. Mater. Interfaces* 6 (2014) 3947–3962.
- [22] Y.C. Shin, J.H. Lee, O.S. Jin, S.H. Kang, S.W. Hong, B. Kim, J.-C. Park, D.-W. Han, Synergistic effects of reduced graphene oxide and hydroxyapatite on osteogenic differentiation of MC3T3-E1 preosteoblasts, *Carbon* 95 (2015) 1051–1060.
- [23] O. Akhavan, E. Ghaderi, M. Shahsavari, Graphene nanogrids for selective and fast osteogenic differentiation of human mesenchymal stem cells, *Carbon* 59 (2013) 200–211.
- [24] W.C. Lee, C.H. Lim, Kenry, C. Su, K.P. Loh, C.T. Lim, Cell-assembled graphene biocomposite for enhanced chondrogenic differentiation, *Small* 11 (2015) 963–969.
- [25] J. Liao, Y. Qu, B. Chu, X. Zhang, Z. Qian, Biodegradable CSMA/PECA/Graphene Porous Hybrid Scaffold for Cartilage Tissue Engineering, *Sci. Rep. UK* 5 (2015).
- [26] K. Yang, L. Feng, Z. Liu, Stimuli responsive drug delivery systems based on nano-graphene for cancer therapy, *Adv. Drug Deliv. Rev.* 105 (2016) 228–241.
- [27] Z. Liu, J.T. Robinson, X. Sun, H. Dai, PEGylated Nanographene oxide for delivery of water-insoluble cancer drugs, *J. Am. Chem. Soc.* 130 (2008) 10876–10877.
- [28] A. Paul, A. Hasan, H. Al Kindi, A.K. Gaharwar, V.T.S. Rao, M. Nikkiah, S.R. Shin, D. Krafft, M.R. Dokmeci, D. Shum-Tim, A. Khademhosseini, Injectable graphene oxide/hydrogel-based angiogenic gene delivery system for Vasculogenesis and cardiac repair, *ACS Nano* 8 (2014) 8050–8062.
- [29] L. Deng, Q. Li, S.a. Al-Rehili, H. Omar, A. Almalik, A. Alshamsan, J. Zhang, N.M. Khashab, Hybrid iron oxide-graphene oxide-polysaccharides microcapsule: a micro-matryoshka for on-demand drug release and antitumor therapy in vivo, *ACS Appl. Mater. Interfaces* 8 (2016) 6859–6868.
- [30] C.L. Weaver, J.M. LaRosa, X. Luo, X.T. Cui, Electrically controlled drug delivery from graphene oxide nanocomposite films, *ACS Nano* 8 (2014) 1834–1843.
- [31] X.J. Loh, T.-C. Lee, Q. Dou, G.R. Deen, Utilising inorganic nanocarriers for gene delivery, *Biomater. Sci. UK* 4 (2016) 70–86.
- [32] Q. Dou, X. Fang, S. Jiang, P.L. Chee, T.-C. Lee, X.J. Loh, Multi-functional fluorescent carbon dots with antibacterial and gene delivery properties, *RSC Adv.* 5 (2015) 46817–46822.
- [33] Y. Chen, L. Wang, J. Shi, Two-dimensional non-carbonaceous materials-enabled efficient photothermal cancer therapy, *Nano Today* 11 (2016) 292–308.
- [34] F. Wang, Q. Sun, B. Feng, Z. Xu, J. Zhang, J. Xu, L. Lu, H. Yu, M. Wang, Y. Li, W. Zhang, Polydopamine-functionalized graphene oxide loaded with gold Nanostars and doxorubicin for combined Photothermal and chemotherapy of metastatic breast cancer, *Adv. Healthc. Mater.* 5 (2016) 2227–2236.
- [35] B. Tian, C. Wang, S. Zhang, L. Feng, Z. Liu, Photothermally enhanced photodynamic therapy delivered by nano-graphene oxide, *ACS Nano* 5 (2011) 7000–7009.
- [36] J. Yu, Y.-H. Lin, L. Yang, C.-C. Huang, L. Chen, W.-C. Wang, G.-W. Chen, J. Yan, S. Sawettanun, C.-H. Lin, Improved anticancer photothermal therapy using the bystander effect enhanced by antiarrhythmic peptide conjugated dopamine-modified reduced graphene oxide nanocomposite, *Adv. Healthc. Mater.* 6 (2017) 1600804.
- [37] O.A. Savchuk, J.J. Carvajal, J. Massons, M. Aguilo, F. Diaz, Determination of photothermal conversion efficiency of graphene and graphene oxide through an integrating sphere method, *Carbon* 103 (2016) 134–141.
- [38] J. Liu, Y. Li, Y. Li, J. Li, Z. Deng, Noncovalent DNA decorations of graphene oxide and reduced graphene oxide toward water-soluble metal-carbon hybrid nanostructures via self-assembly, *J. Mater. Chem.* 20 (2010) 900–906.
- [39] E.P. Randviir, D.A.C. Brownson, C.E. Banks, A decade of graphene research: production, applications and outlook, *Mater. Today* 17 (2014) 426–432.
- [40] M. Verdanova, B. Rezek, A. Broz, E. Ukrainsev, O. Babchenko, A. Artemenko, T. Izak, A. Kromka, M. Kalbac, M.H. Kalbacova, Nanocarbon allotropes-graphene and nanocrystalline diamond-promote cell proliferation, *Small* 12 (2016) 2499–2509.
- [41] M.H. Kalbacova, M. Verdanova, A. Broz, A. Vetushka, A. Fejfar, M. Kalbac, Modulated surface of single-layer graphene controls cell behavior, *Carbon* 72 (2014) 207–214.
- [42] Y. Luo, H. Shen, Y. Fang, Y. Cao, J. Huang, M. Zhang, J. Dai, X. Shi, Z. Zhang, Enhanced proliferation and osteogenic differentiation of mesenchymal stem cells on graphene oxide-incorporated electrospun poly(lactic-co-glycolic acid) nanofibrous mats, *ACS Appl. Mater. Interfaces* 7 (2015) 6331–6339.
- [43] J. Ruan, X. Wang, Z. Yu, Z. Wang, Q. Xie, D. Zhang, Y. Huang, H. Zhou, X. Bi, C. Xiao, P. Gu, X. Fan, Enhanced physicochemical and mechanical performance of chitosan-grafted graphene oxide for superior osteoinductivity, *Adv. Funct. Mater.* 26 (2016) 1085–1097.
- [44] T. Peters Jr., Serum albumin, *Adv. Protein Chem.* 37 (1985) 161–245.
- [45] D.C. Marcano, D.V. Kosynkin, J.M. Berlin, A. Siniitskii, Z. Sun, A. Slesarev, L.B. Alemany, W. Lu, J.M. Tour, Improved synthesis of graphene oxide, *ACS Nano* 4 (2010) 4806–4814.
- [46] J. Shen, M. Shi, B. Yan, H. Ma, N. Li, Y. Hu, M. Ye, Covalent attaching protein to graphene oxide via diimide-activated amidation, *Colloids Surf. B* 81 (2010) 434–438.
- [47] K. Grintzalis, C.D. Georgiou, Y.-J. Schneider, An accurate and sensitive Coomassie brilliant blue G-250-based assay for protein determination, *Anal. Biochem.* 480 (2015) 28–30.
- [48] A.V. Murugan, T. Muraliganth, A. Manthiram, Rapid, facile microwave-solvothermal synthesis of graphene nanosheets and their polyaniline nanocomposites for energy storage, *Chem. Mater.* 21 (2009) 5004–5006.
- [49] L. Ma, G. Wang, J. Dai, Influence of structure of amines on the properties of amine-modified reduced graphene oxide/polyimide composites, *J. Appl. Polym. Sci.* 133 (2016) 43820.
- [50] T. Nguyen Dien Kha, J. Choi, C.R. Park, H. Kim, Remarkable conversion between n- and p-type reduced graphene oxide on varying the thermal annealing temperature, *Chem. Mater.* 27 (2015) 7362–7369.
- [51] W. Chen, L. Yan, P.R. Bangal, Preparation of graphene by the rapid and mild thermal reduction of graphene oxide induced by microwaves, *Carbon* 48 (2010) 1146–1152.
- [52] T. Ramanathan, F.T. Fisher, R.S. Ruoff, L.C. Brinson, Amino-functionalized carbon nanotubes for binding to polymers and biological systems, *Chem. Mater.* 17 (2005) 1290–1295.
- [53] W. Norde, C.E. Giacomelli, BSA structural changes during homomolecular exchange between the adsorbed and the dissolved states, *J. Biotechnol.* 79 (2000) 259–268.
- [54] C.S. Chen, J.L. Alonso, E. Ostuni, G.M. Whitesides, D.E. Ingber, Cell shape provides global control of focal adhesion assembly, *Biochem. Biophys. Res. Commun.* 307 (2003) 355–361.
- [55] M. Kalbacova, A. Broz, M. Kalbac, Influence of the fetal bovine serum proteins on the growth of human osteoblast cells on graphene, *J. Biomed. Mater. Res. A* 100A (2012) 3001–3007.
- [56] J.D. Humphries, P. Wang, C. Streuli, B. Geiger, M.J. Humphries, C. Ballestrem, Vinculin controls focal adhesion formation by direct interactions with talin and actin, *J. Cell Biol.* 179 (2007) 1043–1057.
- [57] W.H. Goldmann, D.E. Ingber, Intact vinculin protein is required for control of cell shape, cell mechanics, and rac-dependent lamellipodia formation, *Biochem. Biophys. Res. Commun.* 290 (2002) 749–755.
- [58] J. Rajeswari, G. Pande, The significance of alpha 5 beta 1 integrin dependent and independent actin cytoskeleton organization in cell transformation and survival, *Cell Biol. Int.* 26 (2002) 1043–1055.
- [59] D. Docheva, C. Popov, W. Mutschler, M. Schieker, Human mesenchymal stem cells in contact with their environment: surface characteristics and the integrin system, *J. Cell. Mol. Med.* 11 (2007) 21–38.
- [60] J. Lee, B.S. Kang, B. Hicks, T.F. Chancellor Jr., B.H. Chu, H.-T. Wang, B.G. Keselowsky, F. Ren, T.P. Lele, The control of cell adhesion and viability by zinc oxide nanorods, *Biomaterials* 29 (2008) 3743–3749.